Supplemental Information for

Free Volume Element Sizes and Dynamics in Polystyrene and Poly(methyl methacrylate) Measured with Ultrafast Infrared Spectroscopy

Sebastian M. Fica-Contreras[a], David J. Hoffman[a], Junkun Pan[a], Chungwen Liang[b], and Michael D. Fayer[a]*

[a]Department of Chemistry
Stanford University, Stanford, CA 94305
*Phone: 650 723-4446; Email: fayer@stanford.edu

[b]Computational Modeling Core Facility, Institute for Applied Life Sciences
University of Massachusetts Amherst, Amherst, MA 01003

*Michael D. Fayer
Phone: (650) 723 – 4446; Email: fayer@stanford.edu

A. Nuclear Magnetic Resonance (NMR) spectroscopy

NMR was used to quantify the solvent and vibrational probe content of the polystyrene (PS) and poly(methyl methacrylate) (PMMA) films. After drying the films in a vacuum oven (see experimental procedures), a 25 mg piece was cut off and dissolved in the appropriate solvent, and its ^{1}H NMR spectrum collected. The PMMA film was dissolved in deuterated acetone, whereas PS was dissolved in deuterated dichloromethane.

All spectra were collected in a 400 MHz Varian NMR spectrometer, using the VNMRJ 4.2 software. A time delay, D1, of 60 seconds was used to avoid diminishing the chloroform signal as a result of the slow relaxation time, T_1, of chloroform in high-density solvents. Standard solutions of known polymer and chloroform content were measured to ensure that quantification was possible. All spectra were analyzed using MNova 12.1.2 from Mestrelab Research. The spectra were phased and baselined using a polynomial fit. The chloroform peak was integrated relative to the methyl ester proton peak of PMMA and the aromatic protons of PS. The areas were normalized to the number of protons that give rise to each signal, and the percent chloroform was calculated with respect to the number of monomers in the polymers. The same procedure was followed to quantify the percent vibrational probe content of the films.

The solvent content of the films was found to be important, since the molecular dynamics presented in this study are highly sensitive to the probe's chemical environment. A higher solvent concentration was found to increase the extent of reorientation of PhSeCN. PMMA was

observed to be more sensitive than PS. The polarization-selective pump-probe (PSPP) measurement was repeated for a series of polymer films with different concentrations of probe and solvent. In this section, we present the NMR spectra of the films for which final results are presented in the main text. A comparison of films with different solvent and probe content is presented and discussed in section B below.

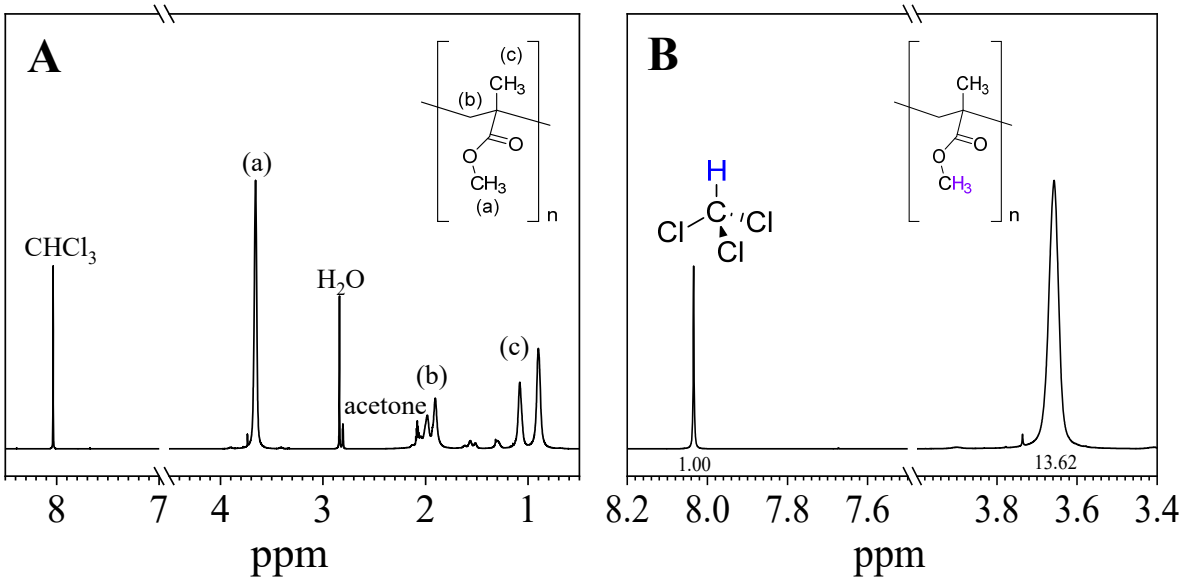

Figure S1. NMR spectra of standard solution of chloroform with PMMA in deuterated acetone. (A) Full ^{1}H NMR spectrum and (B) shows the expanded view of the area of interest. Relevant structures are labeled in blue for chloroform and purple for PMMA.

Fig. S1A shows the full spectrum of the standard solution. The standard sample was made by dissolving 53.7 mg of PMMA and 13.2 mg of chloroform in deuterated acetone. Peaks (a), (b), and (c) were identified with the methyl ester, methylene, and methyl groups of PMMA, respectively. The acetone peak is observed at 2.04 ppm, and it overlaps with the methylene peaks of PMMA. Water was observed at 2.8 ppm. A water signature was observed in the NMR spectrum of the deuterated acetone solvent (not shown), and it was therefore ignored for measurements of experimental samples.

Fig. S1B shows an expanded view of the section of interest of the spectrum in Fig. S1A. The chloroform singlet at 8.04 ppm and the PMMA methyl ester singlet peak at 3.66 ppm are well isolated, and were used for solvent quantification. Integration was performed relative to the area of the chloroform signal (the integral values are shown in Fig. S1B under each peak). Each peak was normalized to the number of protons that generate it and the percent chloroform was calculated. Based on the added mass and molar mass of chloroform (MW 119.38 g/mol) and

PMMA monomer (MW 100.121 g/mol), the expected mol percent chloroform in this solution was calculated as 22.3%. Using the integral values shown in Fig. S1B, the NMR measurement reported a chloroform content of 22.0%. This confirmed that quantification of the chloroform content was possible using this method.

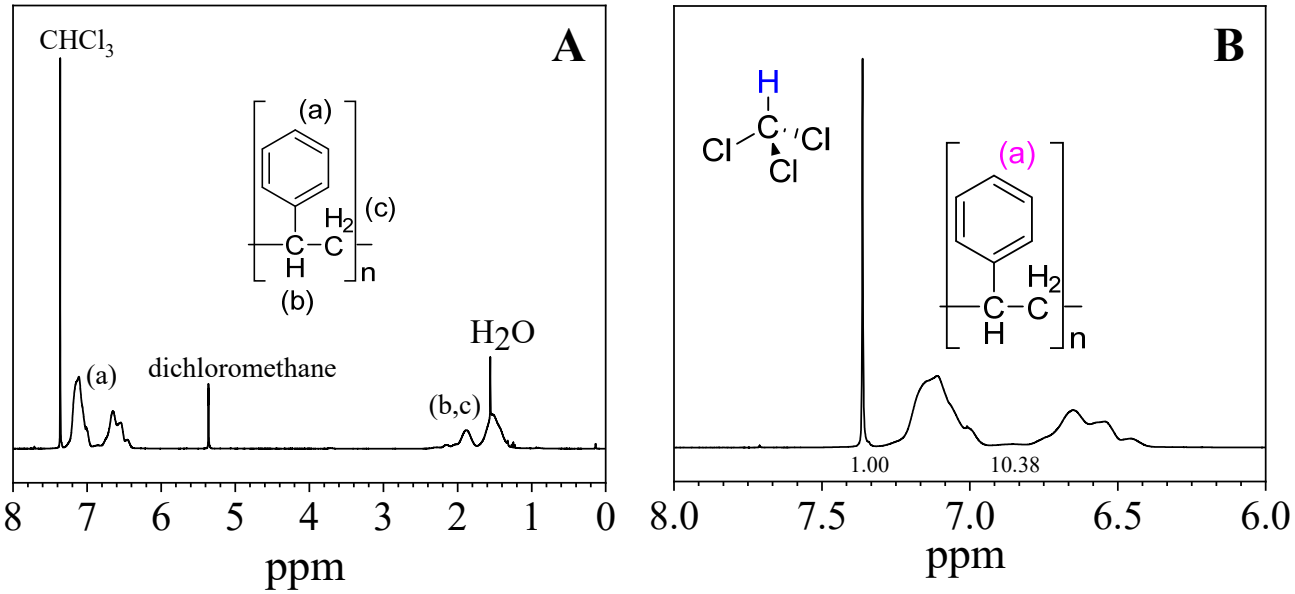

Figure S2. NMR spectra of standard solution of chloroform with PS in deuterated dichloromethane. (A) Full ^{1}H NMR spectrum and (B) expanded view of the area of interest. Relevant structures are labeled in blue for chloroform and magenta for PS.

A similar procedure was followed to confirm our ability to quantify the chloroform content in PS films. Fig. S2A shows the full ^{1}H NMR spectrum of a standard solution of chloroform and PS in deuterated dichloromethane. The peaks labeled (a), and (b, c) correspond to the protons in the aromatic ring of PS, and those in the backbone, respectively. Water was observed in dichloromethane (singlet at 1.5 ppm) and it overlaps with the PS signal.

Due to the overlap of the water and alkyl PS peaks, the signal from the aromatic ring of PS was used for the quantification of chloroform. Following the same procedure outlined above for PMMA, a standard solution was made with 27.0 mg of PS and 15.2 mg of chloroform in deuterated dichloromethane. Using the molar mass of chloroform and the PS monomer (MW = 104.15 g/mol), the expected mol percent of chloroform in the film is 49.0 %. Using the integral values displayed in Fig. S1B, and by normalizing the peaks to the number of protons that generate them, NMR reported a chloroform content of 48.2%. This confirmed our ability to quantify the chloroform content in PS films.

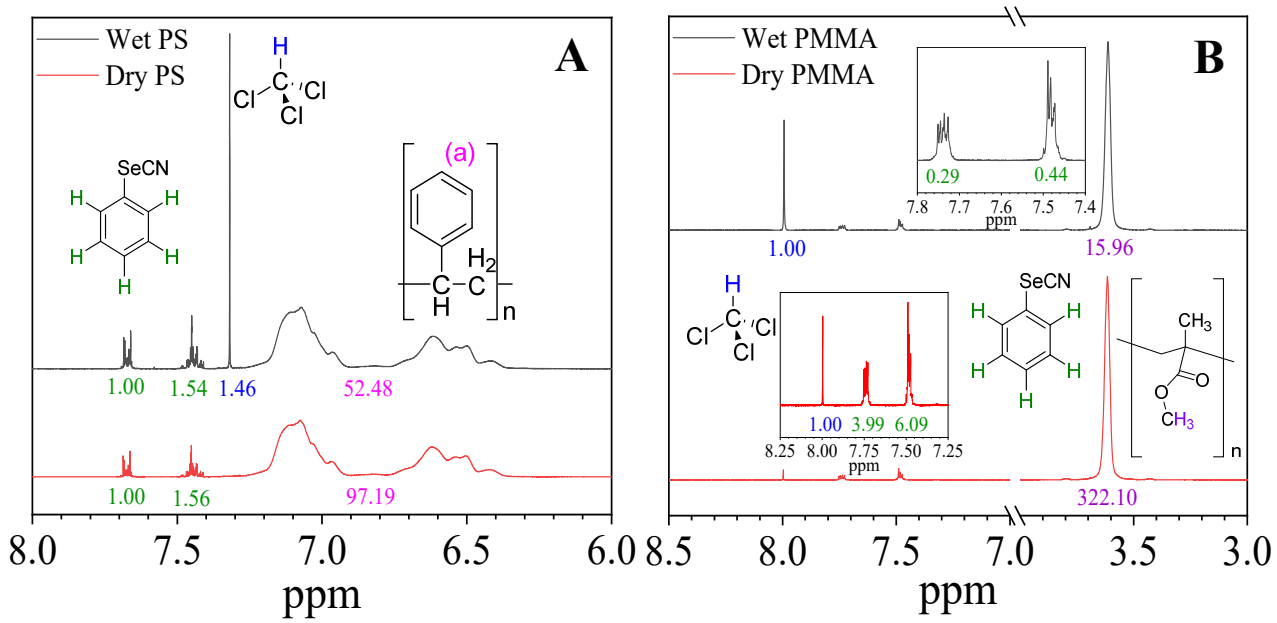

Figure S3. NMR spectra of wet (black) and dry (red) (A) PS and (B) PMMA films. Relevant molecular structures for PhSeCN (green), chloroform (blue), PS (magenta), and PMMA (purple) are included. The colored numerical labels indicate the integral value of each signal. Insets show expanded views of areas of interest with low-intensity signals for better visualization.

In addition to chloroform and polymer signals, these spectra show the PhSeCN probe at 7.45 and 7.68 ppm in deuterated dichloromethane, and 7.48 and 7.74 in deuterated acetone. The PhSeCN peak areas appear in a 2:3 ratio, for a total of 5 protons from the phenyl ring. The NMR spectra were collected before (black) and after (red) drying in a vacuum oven (see main text), and the chloroform and PhSeCN contents were quantified following the procedures described above.

Before drying, the PS film contained 4.8% PhSeCN and 13.9% chloroform. After drying, the PS film showed 2.6% PhSeCN and <0.1% chloroform (this is an estimation, as the peak was almost undetectable). Fig. S3B shows the same measurements for the PMMA film. Insets show an expanded window of the areas of interest with low-intensity peaks for better visualization. Before drying, the PMMA film contained 2.8% PhSeCN and 18.8% chloroform. After drying, the film contained 1.9% PhSeCN and 0.9% chloroform.

B. Orientational dynamics and FVE radii as a function of solvent content

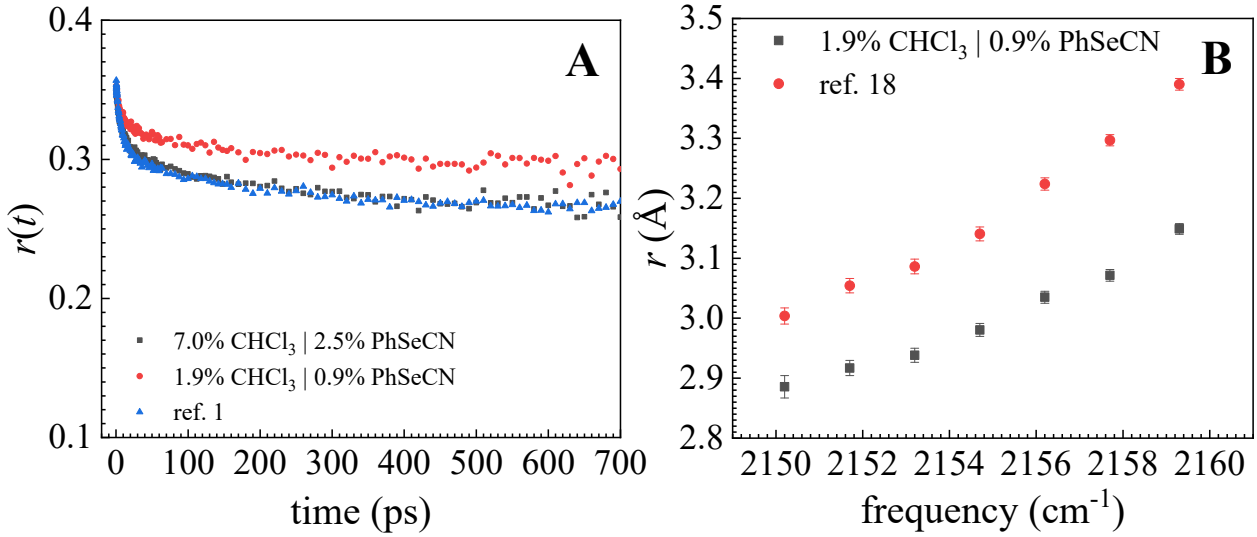

Figure S4. Anisotropy decay for the center frequency (2154.7 cm^{-1}) of PhSeCN in PMMA. (A) Comparison between a film with a known high solvent and probe content, the data presented in previous ROAM publication (ref. 18 in main text), and the results obtained from the dry film presented in this publication. (B) FVE radii obtained from ref. 18 compared to the FVE radii obtained from the dry film presented in the main text.

The orientational dynamics of the vibrational probe are highly sensitive to its chemical environment. Fig. S4A demonstrates that the content of solvent and probe can influence the ROAM measurement. A higher solvent content was associated with a larger extent of orientational dynamics (indicated by a smaller final offset). This likely occurs because the solvent molecules cause the polymer chains to be more mobile, allowing for more reorientation of PhSeCN. Previously, we reported the ROAM analysis on a PMMA film whose solvent content was not quantified using NMR spectroscopy. A retroactive comparison of the data obtained for that film and the present dry film (Fig. S4A, blue triangles vs. red circles) indicates that previously, the PMMA film was not fully dry. Comparison of the data from ref. 18 (in main text) to the anisotropy decay of a film with high solvent content (Fig. S4A, blue triangles vs. black squares) evidenced that our old film contained 7.0% chloroform. The larger extent of probe reorientation that results from a higher solvent content translates into a large FVE radius (Fig. S4B). Previously, we reported an average FVE radius of 3.1 Å for PMMA. Drying the PMMA film thoroughly caused a small decrease in average FVE radius to 3.0 Å. It can be seen in Fig. S4B that chloroform does not affect all FVE equally. At the highest and lowest vibrational frequencies, a 7.1% and a 3.9% decrease in FVE radius was observed, respectively. Such a difference in FVE radii is comparable to the difference in FVE radii across different polymers.

These observations demonstrate that it is very important to thoroughly remove the solvent from polymer films to study polymer free volume.

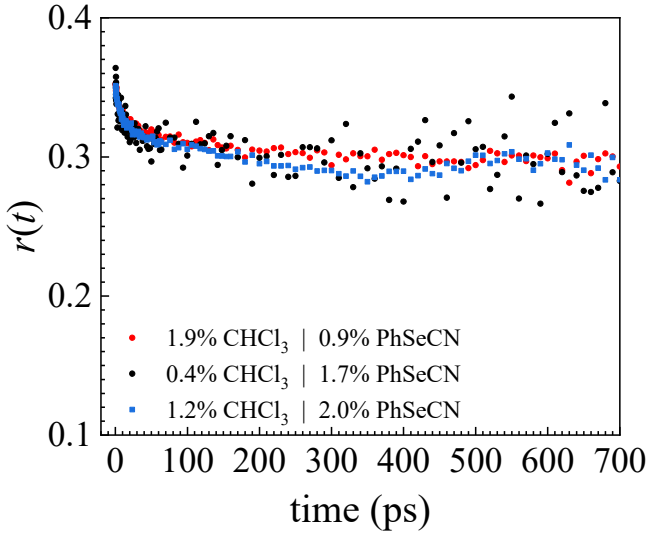

Figure S5. Comparison of the center frequency anisotropy decay of PhSeCN in PMMA obtained from the dry film presented in the main text and those from two additional PMMA films: one with higher and one with lower cumulative solvent/probe concentration.

It was necessary to confirm that the solvent and probe content of the film presented in the main text did not influence the observed dynamics. The PSPP experiment was repeated on a film with higher (1.2% $CHCl_3$ and 2.0% PhSeCN) and lower (0.4% $CHCl_3$ and 1.7% PhSeCN) cumulative solvent/probe concentration. The results from these films are compared to the data from the main text (1.9% $CHCl_3$ and 0.9% PhSeCN) in Fig. S5. It can be seen that all three data sets agreed with each other, suggesting that, within these low bounds of solvent and probe concentration, ROAM is able to report dynamics that are independent of the content of foreign molecules in the polymer matrix.

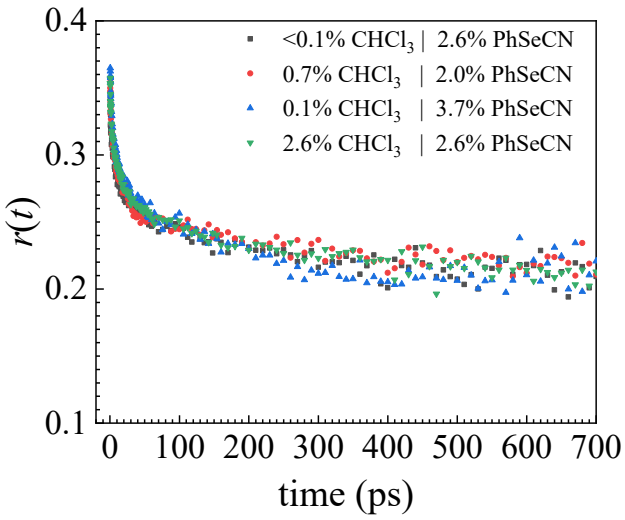

Figure S6. Anisotropy decay for the center frequency (2154.7 cm^{-1}) of PhSeCN in PS. The data were obtained from a variety of films with different chloroform and probe contents.

The data presented in the main text were obtained from the film with <0.1% chloroform and 2.6% PhSeCN (Fig. S6, black squares). The measurement was repeated on a series of other films and the results were compared to ensure no contamination by the presence of solvent and probe molecules occurred. It was observed that the ROAM experiment is robust to cumulative concentration of non-polymer molecules of at least 5.2% in PS. This observation confirms that the results presented in the main text of this work are not influenced by the presence of solvent and vibrational probe in the PS matrix.

C. PhSeCN population lifetime decay

The experimental time-window of the PSPP experiment is limited by the lifetime of the vibrational probe molecule. A long lifetime increases the experimental time-window to observe dynamics. The population decays (Fig. S7) were fit with a single exponential decay function and the lifetime of PhSeCN was determined to be 437 ± 0.4 ps in PS and 434 ± 0.6 ps in PMMA. Compared to other nitriles, PhSeCN has a long-lived first vibrationally excited state, which is attributed to the selenium atom because its large mass. The selenium atom decouples the CN from the phenyl ring, thus disrupting intramolecular relaxation pathways, which increases the excited state lifetime.

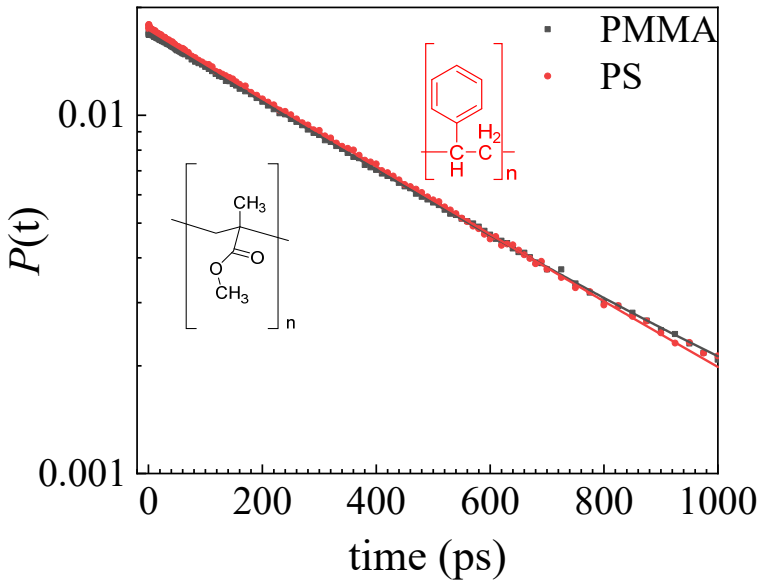

Figure S7. Population lifetime decay, $P(t)$, of PhSeCN in PS (red) and PMMA (black). y-axis is set as a logarithmic scale. Both decays are best described by a single exponential decay function (fits shown as a solid lines).

D. Parameterization of orientational relaxation dynamics

The anisotropy decay curves of PhSeCN in PS and PMMA are described by a biexponential decay to a constant final offset. The fitting function has the following functional form:

$$r(t) = A_1 e^{(-t/\tau_1)} + A_2 e^{(-t/\tau_2)} + y_0 \qquad \text{(S1)}$$

Summaries of the fitting parameters are presented in Tables S1 and S2.

Table S1. Parameterization of the frequency-dependent anisotropy decays in PS using a biexponential decay to an offset.

Frequency (cm^{-1})	A_1	τ_1	A_2	τ_2	y_0
2159.3	0.094 ± 0.004	9.0 ± 0.8	0.077 ± 0.003	196 ± 22	0.15 ± 0.002
2157.7	0.082 ± 0.004	8.1 ± 0.9	0.067 ± 0.003	166 ± 21	0.18 ± 0.002
2156.2	0.070 ± 0.004	8.1 ± 1.1	0.063 ± 0.003	173 ± 25	0.20 ± 0.002
2154.7	0.062 ± 0.004	7.6 ± 1.2	0.060 ± 0.003	171 ± 26	0.21 ± 0.002
2153.2	0.056 ± 0.004	6.6 ± 1.2	0.057 ± 0.003	153 ± 23	0.22 ± 0.002
2151.7	0.052 ± 0.004	6.1 ± 1.2	0.060 ± 0.003	152 ± 22	0.22 ± 0.002
2150.2	0.051 ± 0.004	5.1 ± 1.1	0.061 ± 0.003	137 ± 18	0.23 ± 0.002

Table S2. Parameterization of the frequency-dependent anisotropy decays in PMMA using a biexponential decay to an offset.

Frequency (cm^{-1})	A_1	τ_1	A_2	τ_2	y_0
2159.3	0.047 ± 0.002	8.5 ± 0.8	0.045 ± 0.001	234 ± 29	0.26 ± 0.002
2157.7	0.041 ± 0.002	8.2 ± 0.9	0.037 ± 0.001	199 ± 27	0.27 ± 0.001
2156.2	0.035 ± 0.002	8.0 ± 1.1	0.033 ± 0.002	184 ± 28	0.28 ± 0.001
2154.7	0.028 ± 0.002	7.1 ± 1.2	0.028 ± 0.002	156 ± 26	0.30 ± 0.001
2153.2	0.023 ± 0.002	5.8 ± 1.3	0.025 ± 0.002	138 ± 24	0.30 ± 0.001
2151.7	0.018 ± 0.002	5.4 ± 1.5	0.025 ± 0.001	197 ± 37	0.31 ± 0.001
2150.2	0.016 ± 0.003	2.9 ± 1.1	0.024 ± 0.001	203 ± 38	0.31 ± 0.001

As discussed in the main text, extraction of FVE radii from the anisotropy decay curves requires the parameterization of the orientational dynamics using the wobbling-in-a-cone model. The fits were performed using the following equation:

$$C_2(t) = S_0^2\left(S_1^2 + \left(1 - S_1^2\right)\exp(-t/\tau_1)\right)\left(S_2^2 + \left(1 - S_2^2\right)\exp(-t/\tau_2)\right) \quad \text{(S2)}$$

A summary of the fitting parameters are presented in Tables S3 and S4.

Table S3. Parameterization of the frequency-dependent anisotropy decays in PS using the wobbling-in-a-cone model.

Frequency (cm^{-1})	S_0^2	S_1^2	τ_1 (ps)	S_2^2	τ_2 (ps)
2159.3	0.80 ± 0.006	0.71 ± 0.009	8.5 ± 0.7	0.67 ± 0.009	162.1 ± 18
2157.7	0.83 ± 0.006	0.76 ± 0.009	7.8 ± 0.7	0.73 ± 0.008	145.4 ± 18
2156.2	0.82 ± 0.006	0.79 ± 0.009	7.9 ± 0.9	0.76 ± 0.008	157.6 ± 23
2154.7	0.83 ± 0.006	0.82 ± 0.009	7.5 ± 0.9	0.78 ± 0.008	161.9 ± 25
2153.2	0.84 ± 0.007	0.83 ± 0.009	6.9 ± 0.9	0.79 ± 0.008	164.8 ± 27
2151.7	0.83 ± 0.007	0.84 ± 0.009	6.7 ± 0.9	0.78 ± 0.009	178.2 ± 28
2150.2	0.84 ± 0.007	0.84 ± 0.008	5.9 ± 0.9	0.78 ± 0.009	181.9 ± 28

Table S4. Parameterization of the frequency-dependent anisotropy decays in PMMA using the wobbling-in-a-cone model.

Frequency (cm^{-1})	S_0^2	S_1^2	τ_1 (ps)	S_2^2	τ_2 (ps)
2159.3	0.87 ± 0.003	0.87 ± 0.004	7.4 ± 0.5	0.87 ± 0.003	161.6 ± 15
2157.7	0.88 ± 0.003	0.89 ± 0.004	7.3 ± 0.6	0.89 ± 0.003	145.5 ± 14
2156.2	0.88 ± 0.002	0.90 ± 0.004	7.3 ± 0.8	0.90 ± 0.003	146.0 ± 16
2154.7	0.88 ± 0.003	0.92 ± 0.004	6.5 ± 0.9	0.92 ± 0.003	131 ± 16
2153.2	0.88 ± 0.003	0.94 ± 0.004	5.4 ± 0.9	0.92 ± 0.003	120.0 ± 15
2151.7	0.88 ± 0.004	0.95 ± 0.004	4.4 ± 0.9	0.93 ± 0.003	141.6 ± 18
2150.2	0.88 ± 0.006	0.95 ± 0.006	2.6 ± 0.7	0.93 ± 0.002	151.0 ± 20

E. Calculating the FVE Size Probability Distributions

The ROAM observable is the average radius of the FVEs with a particular frequency of the CN stretch of the probe molecule. This can be expressed as an expectation value

$$\langle r(\omega) \rangle = \int_0^\infty \rho(r \mid \omega) r dr \,, \tag{S3}$$

where $\rho(r|\omega)$ is a conditional probability density function (PDF) corresponding to the probability of a probe being in an FVE of radius r given that it has a frequency ω. The conditional probability distribution relates to the desired FVE distribution, $\rho(r)$, by:

$$\rho(r) = \int_0^\infty \rho(r \mid \omega) \rho(\omega) d\omega \,, \tag{S4}$$

where $\rho(\omega)$ is the probability distribution of probe frequencies (area normalized FT-IR absorption spectrum). From Eq. S4, it should then be possible to determine $\rho(r)$ if the $\rho(r|\omega)$ distributions can be determined. However, the moments of $\rho(r|\omega)$, besides the average, are unknown, making it necessary to have additional information to determine the correct distributions for the subensembles. For instance, the measured standard deviation must be less than a, as the probe molecule cannot report FVE radii smaller than Δr or larger than $\Delta r + a$ per Eq. 5. However, that bound (a = 3.85 Å) is extremely large relative to the range of values sampled by $\langle r(\omega) \rangle$ (~0.3 Å, see Fig. 3). Additionally, as $\rho(r)$ itself has often been described as

non-Gaussian in the literature, it is similarly likely that the subensembles $\rho(r|\omega)$ are non-Gaussian, which would require the determination of even higher moments.

By contrast, vibrational frequency distributions are often well described by Gaussian functions. Even in PMMA, the spectrum is close to Gaussian (Fig. 1B). If it was possible to measure the spectrum associated with a subensemble of FVEs with a single size, the spectral distribution is likely to be well behaved, e.g., a Gaussian. This provides an additional constraint which can be used in calculating the FVE radii distribution. Using Bayes' Theorem, we can relate the conditional PDF $\rho(r|\omega)$ for the radius at a given frequency to these related distributions as follows:

$$\rho(r \mid \omega) = \frac{\rho(\omega \mid r)\rho(r)}{\rho(\omega)} \tag{S5}$$

and

$$\rho(\omega) = \int_0^\infty \rho(\omega \mid r)\rho(r)dr\,, \tag{S6}$$

where $\rho(\omega|r)$ is a conditional PDF corresponding to the probability of a probe emitting at frequency ω given it is in an FVE of radius r. Eq. S3 can then be rewritten as:

$$\left\langle r(\omega)\right\rangle = \frac{1}{\rho(\omega)}\int_0^\infty \rho(\omega \mid r)\rho(r)rdr\,. \tag{S7}$$

The procedure for determining candidate $\rho(r)$ from Eqs. S6 and S7 goes as follows. As both $\rho(r)$ and $\rho(\omega|r)$ are unknown, we will assume a functional form for $\rho(\omega|r)$ and solve for a $\rho(r)$ which satisfies Eq. S6 using the experimental FT-IR absorption spectrum $\rho(\omega)$ (Fig. 1). Using the calculated $\rho(r)$, the frequency-dependent average radii $\left\langle r(\omega)\right\rangle$ can be calculated and compared to the experimental values (Fig. 3). The behavior of $\rho(\omega|r)$ will then be iterated to obtain a set of $\rho(\omega|r)$ and $\rho(r)$ which match both the experimental FT-IR spectrum and the measured FVE radii. Requiring the fits to simultaneously reproduce both the measured radii and the absorption spectrum greatly constrains the results. Towards this end, we will assume the $\rho(\omega|r)$ PDFs are Gaussian, with radius-dependent center frequencies and standard deviations.

As before, the values of the moments of $\rho(\omega|r)$ are poorly constrained, so a variety of behaviors were considered. For both PMMA and PS, a significant step in frequency corresponds to a significant change in radius. The deviation from this behavior for small radii measured at

low frequency requires a nonlinear relationship between radius and frequency.[1] The model used needs to incorporate at least one of the following in its description of $\rho(\omega|r)$: (1) a very small change in radius in the low frequency regime results in a large change in the average vibrational frequency, or (2) the standard deviation of the frequency associated with a particular radius increases with decreasing radii. In either case, a change in frequency in the low frequency regime does not result in the significant change of radius observed at high frequency.

Once functional forms for $\rho(\omega|r)$ are chosen, $\rho(r)$ can be calculated using Eq. S6 and the maximum entropy method, as $\rho(\omega)$ is known from the FT-IR spectrum. After discretizing $\rho(\omega)$, this gives:

$$\rho(r) = \exp\left(\sum_{j=0}^{n} \lambda_j \rho(\omega_j | r) \right). \tag{S8}$$

The Lagrange multipliers λ come from solving the minimization problem:

$$\min\left(\left[\int_0^{\infty} dr \exp\left(\sum_{j=0}^{n} \lambda_j \rho(\omega_j | r) \right) \right] - \sum_{j=0}^{n} \lambda_j \rho(\omega_j) \right). \tag{S9}$$

With $\rho(\omega|r)$ defined and $\rho(r)$ determined, Eq. S7 can be calculated through numerical integration techniques.

F. Polystyrene Oligomer

A PS oligomer (MW 580 Da, MW/Mn 1.12) was purchased from Agilent Technologies and used without further purification. Due to its high viscosity, the oligomer was heated to 100 ℃ and PhSeCN was dissolved in it at a concentration of 2.5 mol % with respect to the monomer unit. The solution was stirred overnight to achieve a homogeneous concentration and deposited between two CaF_2 windows separated by a 250 μm Teflon spacer and put in a temperature-controlled copper cell. An advantage of this sample is that it does not require using any solvent to make it, and it therefore ensures the observation of native oligomer behaviors. Figure S8 displays anisotropy data for the PS oligomer as a function of wavelength at 260 K, which is close to the glass transition temperature of ~240 K. The anisotropy data on the oligomer displays the behavior that is qualitatively identical to that of the high molecular weight PS polymer below its glass transition (see Fig. 2 of the mail text).

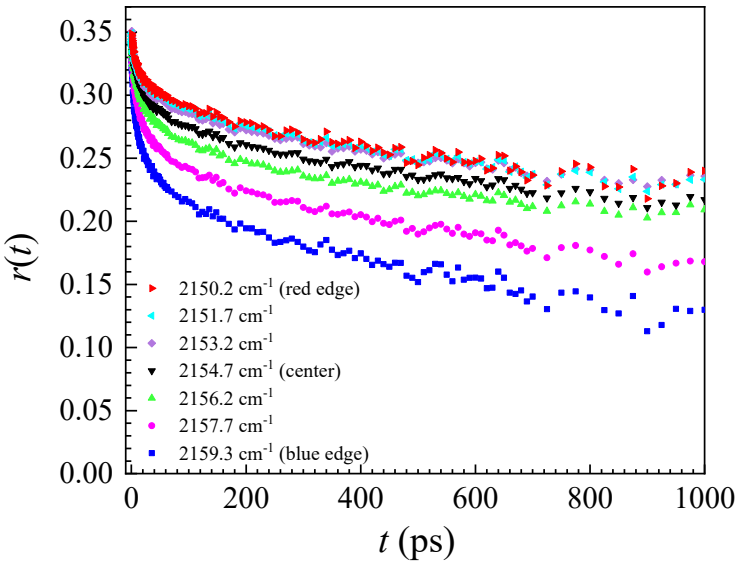

Figure S8. Anisotropy decay as a function of frequency for PhSeCN in MW 580 polystyrene at 260 K. The frequency dependence of the anisotropy decays is qualitatively the same as the high molecular weight polymer (see Fig. 2, main text).

The anisotropy decays are frequency dependent. Anisotropy curves at high frequency decay more than those at low frequency. In addition, at low frequency, the difference in nearby decays decreases, and for the lowest three frequencies, the decays are virtually identical. The features were also observed for a PMMA oligomer and a high MW PMMA film (not shown). As discussed below, the PS oligomer data were quantitatively reproduced by molecular dynamics simulations, and the results confirmed the use of Model 2 for the determination of the FVE radius probability density functions (see Fig. 6 of the main text). A comparison of simulated data to the center frequency (2154.7 cm^{-1}) anisotropy decay of PhSeCN in the PS oligomer at 260 K is given in Fig. S9.

G. Molecular Dynamics Simulations

To provide a detailed molecular picture of polymer systems, atomistic molecular dynamics (MD) simulations of a PS oligomer (5 monomer units) were performed at 260 K using the GROMACS 2018 package.[2] The OPLS force field was chosen for modeling the oligomer and the PhSeCN probe with the modified Lennard-Jones parameters.[3] The LINCS algorithm was used to constrain bond lengths and angles of all the molecules, allowing an integration time step of 2 fs.[4] Long range electrostatic interactions beyond a cutoff of 1.2 nm were calculated by the Particle-

Mesh-Ewald (PME) method with a grid spacing of 0.12 nm.[5] Short-range repulsive and attractive dispersion interactions were described with the Lennard-Jones potentials, using 1.2 nm for the cutoff length. The simulation system contains 512 PS oligomer molecules and 64 PhSeCN probes in a cubic box with a volume of $(7.58\ nm)^3$. The system density was chosen to reproduce the pure PS oligomer density at 260 K (1.18 g/mL).[6] The initial configuration was constructed as follows: after steepest descent energy minimization, 100 ns NVT simulation was performed using Berendsen thermostat to heat up the system at 500 K.[7] This was followed by a 200 ns NVT simulation at 260 K. The 10 ns production run was performed using the velocity rescaling method with an external heat bath at 260 K (coupling time 1 ps).[8]

The Lennard-Jones potentials of PS oligomer and PhSeCN atoms were modified (Table S5) to correctly describe the polymer dynamics and reproduce experimental orientational dynamics of PhSeCN.

Table S5. Lennard-Jones potentials of PS oligomer and PhSeCN atoms

atom	sigma (nm)	epsilon (kJ/mol)
C	0.35	0.12
H	0.25	0.025
N	0.32	0.14
Se	0.51	0.079

A comparison of the experimental orientational dynamics and the simulation results is presented in Fig. S9 and it can be seen that the simulation quantitatively reproduces the experimental data.

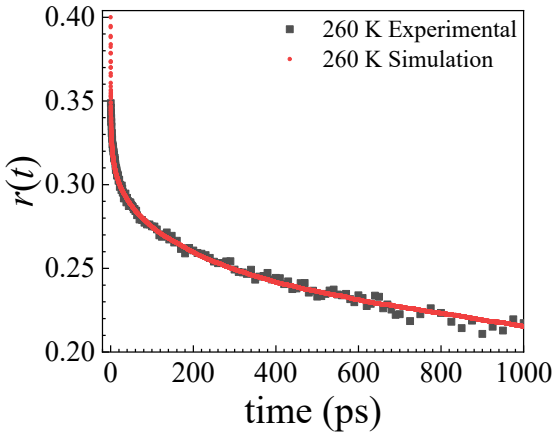

Figure S9. Anisotropy decay of PhSeCN in a PS oligomer is presented at 260 K. The red circles, which appear as a line after the shortest times, show simulated orientational dynamics of the same chemical system. It can be seen that MD simulations quantitatively reproduce the experimental data.

Fig. S10 shows the distribution of electric fields associated with individual FVE radii and vice versa, obtained from the MD simulations. At any specific radius, a vertical slice across the contour plot shows the distribution of electric fields associated with that FVE radius, whereas a horizontal slice shows the distribution of FVE radii associated with a particular electric field.

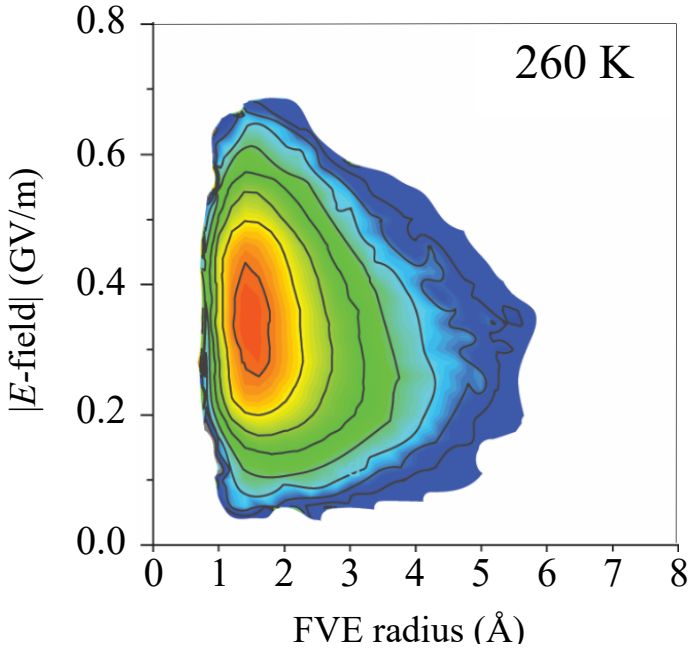

Figure S10. Correlation between electric field strength and FVE radius at 260 K obtained from MD simulations of PhSeCN in a PS oligomer (5 repeat units). For a particular radius, the contour shows a distribution of electric field strengths (frequencies) associated with it (vertical slice) and vice-versa, for a particular *E*-field, there is a distribution of associated radii (horizontal slice).

The vibrational frequency of the CN stretch is determined by the electric field that the surrounding polymer structure generates. Therefore, vibrational frequency and electric field strength are surrogates for one another. The contour plot (Fig. S10) shows that the standard deviation of the distribution of electric fields associated with a particular FVE radius increases with decreasing FVE radius, i.e., the width of a vertical slice becomes larger as the radius becomes small. Each FVE radius represents a subensemble of environments. A particular FVE radius is created by a distribution of polymer configurations, which in turn, generate a distribution of electric fields. Because the electric field determines the vibrational frequency of the probe, a particular probe subensemble is associated with a distribution of vibrational frequencies, and this distribution becomes wider as the radius decreases. Therefore, the MD simulation demonstrates that the standard deviation of the electric field that is associated with each subensemble of probe molecules becomes larger with decreasing FVE radius. This means that the spectral standard deviation increases with decreasing FVE radius. This is exactly the physical underpinning of Model 2 used in the determination of the FVE size probability distribution (Figs. 5 and 6), which is the reason Model 2 was chosen over Model 1.

Looking at horizontal slices in Fig. S10, high electric fields (low frequencies) show narrow distributions of FVE radii in the small FVE radii region, whereas the low fields (high frequencies) shows a broad distribution of FVE radii with tails to large FVE radii. ROAM measures the average FVE radius of the distribution at a particular vibrational frequency (electric field strength) not the peak of the distribution. Because the horizontal slice for a small electric field is broader than for a high electric field, the average radius of each horizontal slice increase with decreasing electric field (lower frequency). Therefore, the MD simulation predicts that the FVE radius reported by ROAM will increase with increasing vibrational frequency. These observations are in qualitative agreement with and validate the trend observed in Fig. 3 in the main text.

H. Maximum Entropy Distributions for PS: alternative Model 1

An alternative model to account for the non-linear relationship between measured FVE radius and frequency (Fig. 3) was considered. In both Models 1 and 2, the center frequencies of $\rho(\omega|r)$ varied at least linearly with FVE radius. While in Model 2 the standard deviation increases with decreasing radius, in Model 1, the center frequency decreased dramatically with decreasing

radius. Fig. S11A shows the joint distribution (Distribution 1), $\rho(\omega,r) = \rho(\omega|r)\,\rho(r)$, obtained from Model 1. The black points are the experimental radii vs. frequency and the red line is the calculated average radii vs. frequency from Eq. S7. For a given radius, the horizontal slice of the contour plot shows the range of frequencies associated with it, $\rho(\omega|r)$. The PS experimental FT-IR spectrum (black dashed curve) and the calculated spectrum (red curve) from Eqs. S8 and S9 are shown in Fig. S11B. Figs. S11A and B show that the experimental data, i.e., the radii and the non-Gaussian absorption spectrum can also be reproduced quantitatively using Model 1.

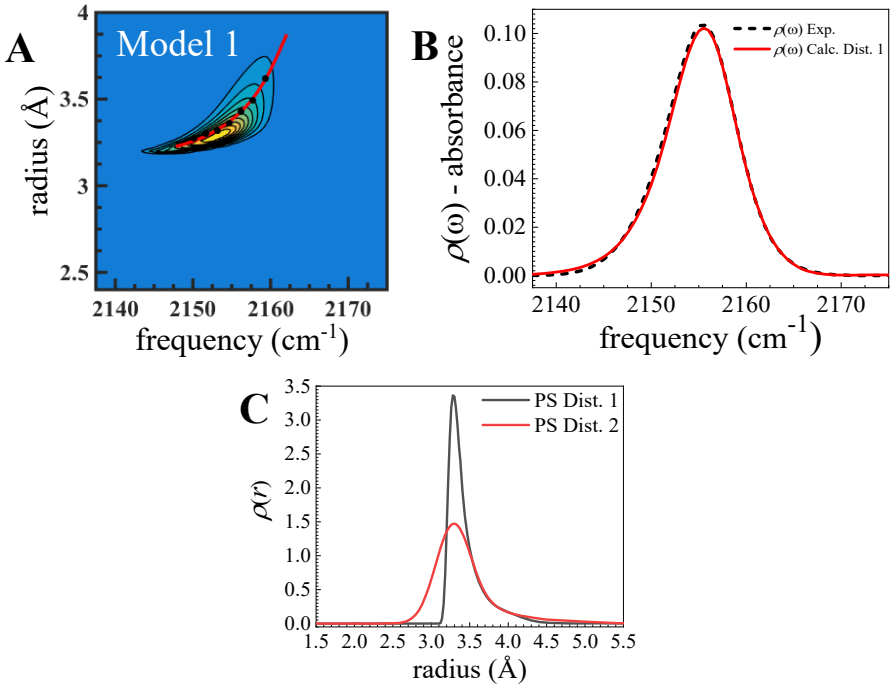

Figure S11. Results of the maximum entropy calculation using Model 1 for the FVE size distribution of PS. In Model 1, the center frequency decreases dramatically as the radius decreased to account for the non-linear relationship between FVE radius and frequency (Fig. 3). (A) Joint probability distributions of FVE radius and probe frequency, $\rho(\omega,r)$, for Model 1. The black points are the measured radii vs. frequency and the solid red curves are the calculated radii vs. frequency. (B) The experimental FT-IR spectrum (black dashed curve) and the calculated spectrum (red solid curve). (C) The area-normalized probability density functions, i.e., the relative probability of an FVE having a particular radius, $\rho(r)$, for the two models. Both peak at the same value and give an identical tail to large radius. Initial molecular dynamics simulations show that Model 2 is the correct model (see above).

Fig. S11C shows a comparison of the resulting FVE radii PDFs obtained from Model 1 and 2. The joint distribution gives a $\rho(r)$ that is sharply peaked at 3.3 Å, which results from the

substantial fraction of small radii measured on the red side of the spectrum. The distributions are not Gaussian and have a tail to larger radii. The tails arise from the larger radii experimentally observed on the blue side of the spectrum. The main difference between the two calculations is that Distribution 1 (from Model 1) has a very steep rising edge on the small side of the radius distribution, while Distribution 2 (from Model 2) has a more gradual rise. The steepness of the rising edge for Model 1 is likely unphysical and is not consistent with literature data for PS. The differences ultimately arise from the different assumptions in the behavior of $\rho(\omega|r)$ at small radii. These calculations demonstrate that by only assuming that the behavior of $\rho(\omega|r)$ is Gaussian, that is, a subensemble of FVEs with a particular radius has a Gaussian spectrum (or any well-behaved spectrum with a single sharp peak), similar FVE radii distributions, $\rho(r)$, can be extracted from the data with the same peak position at small radius and a tail to large radius. However, as explained in Section G above, MD simulations demonstrate that Model 2 is correct, which is the reason Distribution 2 is chosen over Distribution 1.

I. Maximum Entropy Distributions for PMMA

As described in the main text for polystyrene and demonstrated in Figs. 5 and S10, it is possible to determine the FVE radii PDF by taking the experimental absorption spectra and the ROAM observable, and assuming a Gaussian set of sub-ensembles for $\rho(\omega|r)$. Here, the same result is shown for PMMA. Two calculations are shown for different behaviors of the conditional PDF, $\rho(\omega|r)$, which describes the spectra of the subensemble of PhSeCN in an FVE of a certain radius. Dist. 1 has $\rho(\omega|r)$ with a constant standard deviation but sharply decreasing center frequency with decreasing radius, while Dist. 2 has $\rho(\omega|r)$ with a sharply growing standard deviation with decreasing radius. The joint PDFs (Fig. S12A) $\rho(\omega,r)$, show that in spite of the very different assumption in the two cases, both models give average radii (red lines) that describe the experimental data (black points). Additionally, both models quantitatively reproduce the inhomogeneous absorption spectrum (Fig. S12B). In addition, both cases give qualitatively very similar FVE radii distributions (Fig. S12C). For PMMA the deviation from linear behavior shown in Fig. 3 of the main text is much smaller than for PS. The more nearly linear behavior results in the two models producing more similar probability distributions than they do for PS as can be seen in Fig. S12C. Once again, because of the results obtained from MD simulations, Model 2 (Dist. 2) is chosen over Model 1 (Dist. 1).

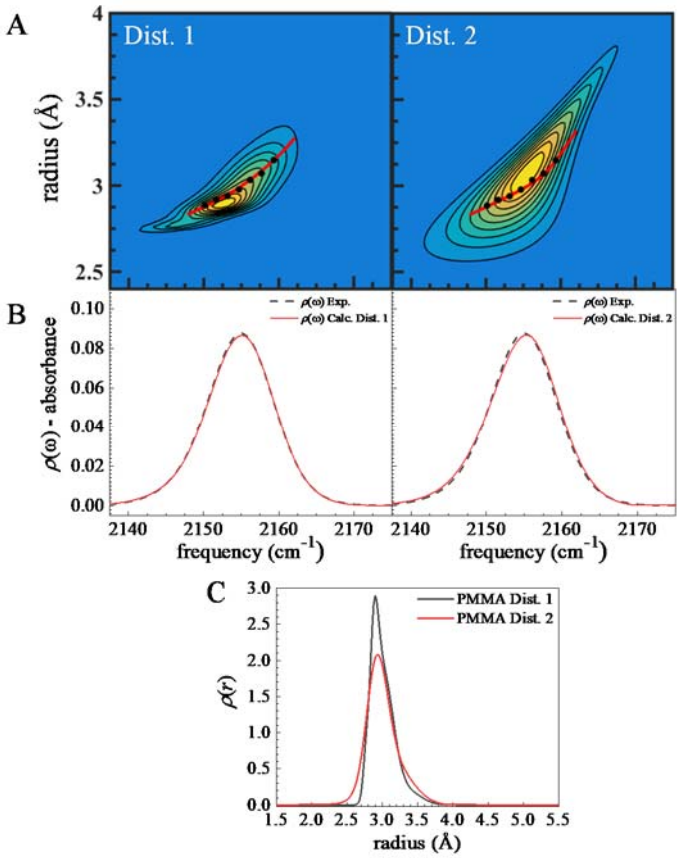

Figure S12. Results of the maximum entropy calculation for the instantaneous FVE distribution of PMMA using two different behaviors of the conditional PDF, $\rho(\omega|r)$. (A) Joint distributions for the two cases, which both describe the data (experiment: black points, calculation: red curves). (B) Experimental (dashed line) and predicted (solid line) absorption spectrum. (C) Resulting distributions (area normalized) for the range of FVE radii, showing that the different cases give nearly the same result.

References

1. Hoffman, D. J.; Fica-Contreras, S. M.; Fayer, M. D., Amorphous polymer dynamics and free volume element size distributions from ultrafast IR spectroscopy. *Proc. Natl. Acad. Sci. U.S.A.* **2020,** *117* (25), 13949-13958.

2. Abrahama, M. J.; Murtolad, T.; Schulzb, R.; Pálla, S.; Smithb, J. C.; Hessa, B.; Lindahl, E., GROMACS: High performance molecular simulations through multi-level parallelism from laptops to supercomputers. *SoftwareX* **2015,** *1-2*, 19-25.

3. Jorgensen, W. L.; Tirado-Rives, J., The OPLS Potential Functions for Proteins. Energy Minimizations for Crystals of Cyclic Peptides and Crambin. *J. Am. Chem. Soc.* **1988,** *110* (6), 1657-1666.

4. Hess, B.; Bekker, H.; Berendsen, H. J. C.; Fraaije, J. G. E. M., LINCS: A Linear Constraint Solver for Molecular Simulations. *J. Comput. Chem.* **1997,** *18* (12), 1463 - 1472.

5. Darden, T.; York, D.; Pedersen, L., Particle mesh Ewald: An N·log(N) method for Ewald sums in large systems. *J. Chem. Phys.* **1993,** *98* (12), 10089 - 10092.

6. Fox, T. G.; Loshaek, S., Influence of Molecular Weight and Degree of Crosslinking on the Specific Volume and Glass Temperature of Polymers. *J. Polym. Sci.* **1955,** *15* (80), 371-390.

7. Berendsen, H. J. C.; Postma, J. P. M.; Gunsteren, W. F. v.; DiNola, A.; Haak, J. R., Molecular dynamics with coupling to an external bath. *J. Chem. Phys.* **1984,** *81* (8), 3684-3690.

8. Bussi, G.; Donadio, D.; Parrinello, M., Canonical sampling through velocity rescaling. *J. Chem. Phys.* **2007,** *126* (1), 014101.